Brandon S. Sargent[1]
Compliant Mechanisms Research Group,
Department of Mechanical Engineering,
Brigham Young University,
Provo, UT 84602
e-mail: bsargent@byu.net

Collin R. Ynchausti
Compliant Mechanisms Research Group,
Department of Mechanical Engineering,
Brigham Young University,
Provo, UT 84602
e-mail: collinynchausti@byu.net

Todd G. Nelson
Department of Engineering,
University of Southern Indiana,
Evansville, IN 47712
e-mail: tgnelson@usi.edu

Larry L. Howell
Compliant Mechanisms Research Group,
Department of Mechanical Engineering,
Brigham Young University,
Provo, UT 84602
e-mail: lhowell@byu.edu

The Mixed-Body Model: A Method for Predicting Large Deflections in Stepped Cantilever Beams

This paper presents a method for predicting endpoint coordinates, stress, and force to deflect stepped cantilever beams under large deflections. This method, the mixed-body model or MBM, combines small deflection theory and the pseudo-rigid-body model for large deflections. To analyze the efficacy of the model, the MBM is compared to a model that assumes the first step in the beam to be rigid, to finite element analysis, and to the numerical boundary value solution over a large sample set of loading conditions, geometries, and material properties. The model was also compared to physical prototypes. In all cases, the MBM agrees well with expected values. Optimization of the MBM parameters yielded increased agreement, leading to average errors of <0.01 to 3%. The model provides a simple, quick solution with minimal error that can be particularly helpful in design.
[DOI: 10.1115/1.4053376]

Keywords: stepped beams, cantilever beams, large deflections, pseudo-rigid-body model, compliant mechanisms

1 Introduction

Beams with stepped cross sections are common, like the stepped cantilever beam shown in Fig. 1(*a*), and there has been extensive research regarding their behavior. This research has occurred in deflection of stepped shafts [1,2], static deflection and vibrational analysis [3], vibrational analysis [4–6], electrostatic microbeams for microelectromechanical systems (MEMS) [7,8], telescoping beams for space applications as demonstrated in Fig. 2 [9,10], and energy harvesting [11,12]. Stepped compliant beams show promise for use in medical implants. A biomedical application, not disclosed in this work, is the primary motivation for this research.

Another instance of stepped beams comes through stepping of material properties. Beams with the same cross section along the length could behave similarly to that of a stepped cross section through stepping down in material stiffness at a discrete point (see Fig. 1(*b*)). As manufacturing methods expand, multi-material beams and mechanisms are becoming increasingly feasible [13–15]. Efficient modeling of beams with steps in geometry and/or material properties undergoing large deflections could enable advances in compliant mechanisms and mechanism design.

Past research is generally focused on small deflections where linear equations are accurate. The transition from small deflections to large deflections is not trivial, even with a simple cantilever beam. To determine analytical expressions for large deflections, elliptic integrals are often necessary [16]. Models, such as the pseudo-rigid-body model (PRBM) [17], have been developed to simplify the analysis and make design of large-deflection beams more feasible, opening up the study of compliant mechanisms. However, many of these approaches generally apply to beams with constant material properties and constant moments of inertia of the cross section [18–20]. It is not uncommon for compliant flexures to be anchored into bodies that are stiffer than the flexure but are not stiff enough to be assumed to be fully rigid. An example of this could be telescoping members (see Fig. 2) where initial members could be considered as relatively stiff, even within the range of deflections such that traditional linear approaches apply, while later members deflect enough to induce geometric nonlinearities.

Nonlinearities come in two forms: material nonlinearities and geometric nonlinearities. Material nonlinearities occur when the stress and strain of the materials are not linearly related, such as plastic deformation or nonlinear material properties. Geometric nonlinearities occur when the deflections change the problem, such as with large deflections. This is well understood in the area of compliant mechanisms [17]. When subsequent discussion of nonlinearities occurs in this paper, it will be discussing the geometric nonlinearities of large bending deflections. Discussion of the linear solution refers to Castigliano's second theorem.

Work in compliant mechanisms has created well-defined models to describe the motion and stresses of cantilever beams undergoing deflections that cause geometric nonlinearities. In all these cases, the attachment or "wall" where the beam attaches is assumed to be perfectly rigid. Of particular interest in this work is the case when the wall attachment cannot be assumed as perfectly rigid

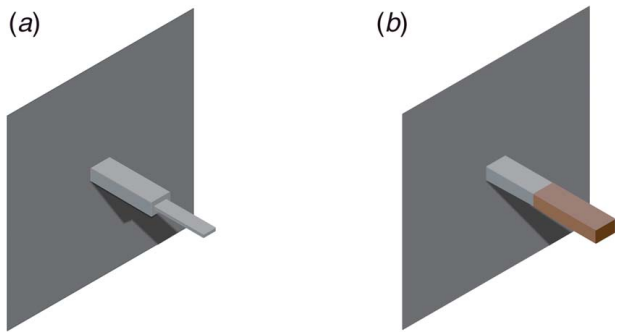

Fig. 1 (*a*) Stepped beam with two different beam cross sections. (*b*) Stepped beam of the same cross section but composed of two materials with different material properties.

[1]Corresponding author.

Contributed by the Mechanisms and Robotics Committee of ASME for publication in the Journal of Mechanisms and Robotics. Manuscript received September 27, 2021; final manuscript received December 15, 2021; published online February 18, 2022. Assoc. Editor: Guangbo Hao.

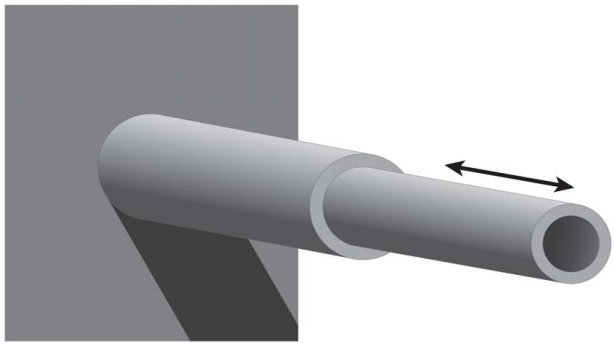

Fig. 2 Example of a telescoping stepped beam geometry

and non-negligible deformation and angle change occurs at the transition from a stiffer segment to a segment with a reduced stiffness. A common example of this is the transition region of an electrical cord into the wall plug. While the plug could be considered as approximating rigid motion, manufacturers often include a stiff segment extending from the plug as a transition from the plug to the cord. The cord is designed for large deflections, while the transition segment is often far more rigid. Models to understand this transition and the stress reduction provided by the stiff segment could improve the design of consumer electronics.

The chain algorithm [17], the beam-constraint-model [21,22], and chained beam-constraint-model [23] provide ways to incorporate differing geometries and material properties when modeling cantilever beams. These models discretize beams into a number of elements (smaller beams) whose deflection is sequentially solved to determine the overall deflection of the beam. These solutions provide valid approaches but often incorporate computational expenses similar to other numerical approaches such as finite element analysis (FEA) or are limited in the deflection range that can be analyzed.

Here, we present an analytical model to analyze stepped cantilever beams undergoing large deflections. The resulting model shows promise for use in design because it can be used to quickly analyze many design choices.

1.1 Background. Large deflections are common in the analysis of compliant mechanisms or mechanisms that gain some or all of their motion through the bending or flexing of material [17]. The flexibility of a beam is in large part determined by the moment of inertia of the cross section of the beam. In stepped beams, the moment of inertia changes with each subsequent step. In small deflections, Castigliano's second theorem is commonly used to determine endpoint deflection of these stepped beams [24]. But expanding to large displacements, another approach needs to be considered. By combining traditional small-deflection theory and the models used to predict motion in large-deflection compliant mechanisms, a method is presented here to predict the behavior of stepped cantilever beams undergoing *s*. The combining of small and large deflection analyses for stepped cantilever beams has been studied previously for numerical solutions [25]. In this work, we consider stepped beams with a single step from a larger moment of inertia near the wall and a smaller moment of inertia towards the tip.

1.1.1 Small-Deflection Theory. The Euler–Bernoulli equation for beams in bending is given by

$$M = EI\frac{d\theta}{ds} \tag{1}$$

where M is the bending moment in the beam, E is the modulus of the elasticity, I is the moment of inertia of the beam, and $d\theta/ds$ is the curvature along the length of the beam.

Small-deflection assumptions allow for simplifications to this equation. These assumptions also allow the use of the principle of superposition to account for multiple forces and moments. These assumptions lead to the deflection of the end of a cantilevered beam with an applied vertical force and moment at the end of the beam as

$$\delta = \frac{FL^3}{3EI} + \frac{ML^2}{2EI} \tag{2}$$

and the end angle is given by

$$\theta = \frac{FL^2}{2EI} + \frac{ML}{EI} \tag{3}$$

where F is the vertical force at the endpoint of the beam, M is an applied bending moment on the beam, and L is the length of the beam.

1.2 Large Deflections. Although small-deflection assumptions simplify calculations and have many applications, they become more inaccurate as the deflections increase. Because the deflections of compliant mechanisms often exceed the valid range of the small-deflection assumptions, large-deflection theory must be used and we have to step back to Eq. (1). The use of elliptic integrals provides an analytical solution for beam-endpoint locations and angles but the complexity of these solutions make them impractical to use in many cases and only numerically solvable in others [16,26–28]. To simplify the design and analysis of compliant mechanisms, the PRBM was developed.

1.2.1 Pseudo-Rigid-Body Model. The PRBM approximates the motion of a large-deflection cantilever beam by approximating the compliant beam with rigid links connected by a pin joint, called a characteristic pivot, with a torsion spring. The motion of the end of the rigid link approximates the motion of the end of the flexible beam [17]. The PRBM has found wide application in the design of mechanisms and structures with large deflections [20,29–37]. Due to the low computational expense of the PRBM, it provides a computationally inexpensive alternative to numerical approaches for design and optimization [38].

Equations (4) and (5) provide the x- and y-distances of the beam end as measured from the coordinate axes, where γ is the characteristic radius factor which defines pseudo-rigid link lengths and the position of the characteristic pivot, l is the length of the beam, and Θ is the pseudo-rigid link angle between the long rigid link and horizontal (see Fig. 3). Note the lowercase of l is used to indicate a segment undergoing large deflections where the uppercase L is used to indicate a segment undergoing small deflections.

$$a = l(1 - \gamma(1 - \cos\Theta)) \tag{4}$$

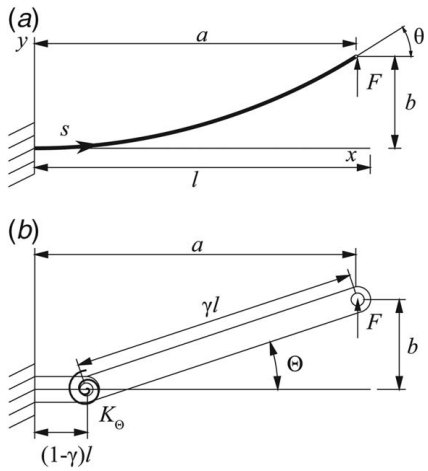

Fig. 3 (*a*) Parameters for large deflection of a cantilever beam under a tip load and (*b*) PRBM and labeled parameters

$$b = l\gamma \sin\Theta \tag{5}$$

Equation (6) relates the force to the angular deflection of the large-deflection beam, where K_Θ is the stiffness coefficient and F is the applied vertical force.

$$Fl\gamma \cos\Theta = \gamma K_\Theta \frac{EI}{l}\Theta \tag{6}$$

The maximum stress in the beam, σ_{max}, is given by Eq. (7), with c being the farthest distance beam fiber from the neutral axis of the beam.

$$\sigma_{max} = \frac{Fac}{I} \tag{7}$$

Presented here are the equations for a cantilever beam with a pure vertical load at the end. The equations used in defining the PRBM in Eq. (6) are the framework for the mixed-body model (MBM). The governing principles behind the parameters used in the PRBM are well known and can be found in greater detail in Ref. [17], including other loading cases and boundary conditions.

2 Materials and Methods

This section details the development of the MBM for stepped cantilevered beams and the accompanying steps taken to validate the model. This includes a comparison to assuming rigidity in the stiffer segment of the beam, the use of FEA, physical testing, and comparisons to numerically solving a boundary value problem (BVP) describing large deflection. For the development of the model, a purely vertical force at the tip of the stepped cantilevered beam is used, as shown in Fig. 4.

2.1 Rigid-Body Assumption for Comparison. To highlight the usefulness of the MBM, the MBM was compared to a stepped beam where the first segment is considered to be infinitely rigid. This effectively moves the origin to the step and from there the flexible segment response can be easily determined using the PRBM (see Fig. 5). The only change is the value for the endpoint in x, a_r, which becomes

$$a_r = l_f(1 - \gamma(1 - \cos\Theta)) + L_s \tag{8}$$

where l_f is the length of the flexible segment and L_s is the length of the segment considered to be rigid corresponding to the origin shift. However, the value of a used in the calculation of the maximum stress in the flexible segment (Eq. (7) in the PRBM) is not a_r as in Eq. (8), but the value of a before the length L_s is added. Therefore, the calculation of stress for the rigid assumption case is given by

$$\sigma_{max} = \frac{F(a_r - L_s)c_f}{I_f} \tag{9}$$

where the subscript f denotes the values referring to the flexible segment of the beam.

2.2 Development of the Mixed-Body Model. The MBM was developed through the combination of the traditional small-deflection assumptions and the use of the PRBM. The small-deflection assumptions are to be applied to the segment of the stepped beam that is attached to the wall. This cross section is thicker than the subsequent step and therefore would be more stiff. The subsequent step is then assumed to have a stiffness low enough to undergo large deflections. The PRBM is applied to this segment. The MBM is shown in Fig. 6 and will be referenced throughout the formulation of the model.

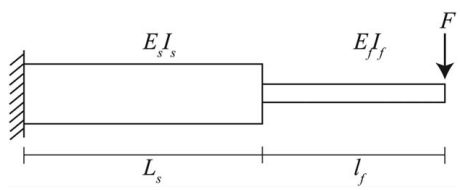

Fig. 4 Example stepped cantilevered beam with a pure vertical force at the tip

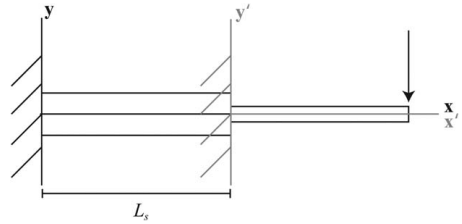

Fig. 5 Example of the application of the rigid assumption with the shift of origin by the length L_s

The PRBM assumes that the flexible beam acts as two pseudo-rigid links with a torsional spring at the characteristic pivot (see Fig. 7). If it is assumed that a force at the tip of the flexible segment would transfer the force the same way as the rigid link system assumed by the PRBM, the characteristic pivot pin joint would feel the same magnitude resultant force as at the tip and a moment caused by the torsional spring. This torsional spring moment at the characteristic pivot would be, as originally formulated in the PRBM [17],

$$M_{ts} = \gamma K_{\Theta f} \frac{E_f I_f}{l_f}\Theta_f \tag{10}$$

with subscripts f representing the flexible segment and ts indicating the torsional spring. A free-body diagram of this pseudo-rigid link is shown in Fig. 8. The equal and opposite moment and force would then be applied to the end of the stiff beam. The length of the stiff segment is no longer just the stiff length, L_s, with the subscript s representing the stiff segment but also includes the length of the flexible segment up to the characteristic pivot (see Fig. 7). As this new length

$$L_{s\gamma} = L_s + l_f(1 - \gamma) \tag{11}$$

is a function of the γ used in the PRBM determination of the characteristic pivot location, the subscript is represented as $s\gamma$. This stiffer segment is shown in Fig. 9.

Using this assumption, the deflection and angle equations for force and moment at the end of a cantilevered beam undergoing small deflections (Eqs. (2) and (3)) become, using superposition,

$$\theta_s = \frac{FL_s}{2E_sI_s}(2L_{s\gamma} - L_s) + \frac{M_{ts}L_s}{E_sI_s} \tag{12}$$

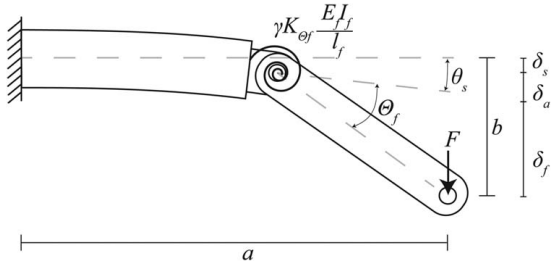

Fig. 6 The beam endpoint locations of the MBM with a vertical load. The respective beam angles and the torsional spring constant are labeled.

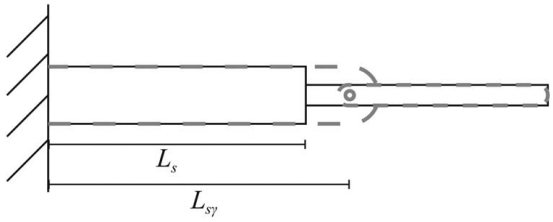

Fig. 7 Demonstration of the MBM approximation of a stepped cantilever beam. The gray dashed lines show the new stiff length, $L_{s\gamma}$, to the characteristic pivot and the pseudo-rigid link.

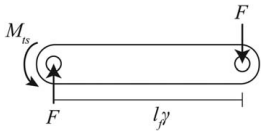

Fig. 8 Free body diagram of the pseudo-rigid-body segment of the MBM. The vertical force on the right is the applied load. The force and moment on the left are the reaction loads at the characteristic pivot.

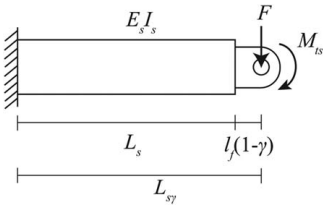

Fig. 9 Stiff segment of the MBM with the reaction loads at the characteristic pivot

$$\delta_s = \frac{FL_s^2}{6E_sI_s}(3L_{s\gamma} - L_s) + \frac{M_{ts}L_s^2}{2E_sI_s} \tag{13}$$

If a load was applied at the characteristic pivot only and the flexible segment remained undeflected, θ_s would add an additional displacement of the endpoint of the stepped beam through changing the undeflected angle of the flexible segment. This deflection, δ_a, or the deflection due to the stiff segment angle, θ_s, is

$$\delta_a = l_f\gamma \sin\theta_s \tag{14}$$

The deflection of the flexible segment remains similar to that predicted by the PRBM (Eq. (5)). To account for the rotation of the flexible segment caused by the deflection of the stiff segment, the traditional vertical deflection PRBM is multiplied by $\cos\theta_s$ and therefore the vertical endpoint deflection of the flexible segment is given as

$$\delta_f = l_f\gamma \sin\Theta_f \cos\theta_s \tag{15}$$

These three deflections can be combined to predict the endpoint deflection b for the MBM. a is also a combination of the respective deflections. They become

$$b = \delta_s + \delta_a + \delta_f \tag{16}$$

$$a = L_s + \cos\theta_s(l_f(1 - \gamma(1 - \cos\Theta_f))) \tag{17}$$

Note that the small-deflection assumption makes no change to the endpoint deflection in the x-direction, contributing the entire length L_s to the value of a. The flexible segment deflection in the x-direction again includes a term to account for the stiff segment angle. The MBM with endpoint deflections and angles labeled is shown in Fig. 6.

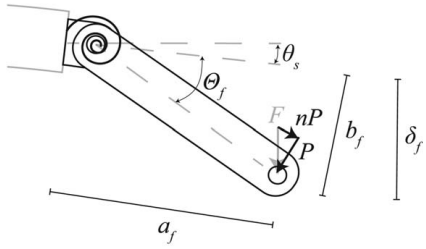

Fig. 10 The flexible segment of the MBM with the loads and dimensions in the reference frame of the flexible segment. This follows the form of a PRBM under combined loading rotated by θ_s.

The maximum stress in the beam will occur at the interface between the flexible and stiff segments or at the wall dependent on the proportions of the geometry as shown in the next subsection. Due to the contribution of θ_s, the pure vertical load has vertical and horizontal components. Following the convention in Ref. [17], the load F becomes P for the component that acts perpendicular to the initial unbent orientation and nP as the parallel component of the force (see Fig. 10). P and n are given as

$$P = F\cos\theta_s \tag{18}$$

$$n = -\tan\theta_s \tag{19}$$

To use the equations for the maximum stress in Ref. [17], the amount that the flexible segment bends from its initial position is required, in components of the perpendicular and parallel lengths. We will call these lengths a_f for the parallel component and b_f for the perpendicular component. These values are given by

$$b_f = l_f\gamma \sin\Theta_f \tag{20}$$

$$a_f = l_f(1 - \gamma(1 - \cos\Theta_f)) \tag{21}$$

and are only a function of geometry and Θ_f. The maximum stress in the flexible section at the step can then be calculated by

$$\sigma_f = \frac{(Pa_f + nPb_f)c_f}{I_f} - \frac{nP}{A_f} \tag{22}$$

where A_f is the cross-sectional area and c_f is the farthest distance beam fiber from the neutral axis of the beam, both for the flexible segment.

2.2.1 Limits of Stress Formula. The maximum stress in the flexible beam due only to bending is

$$\sigma_{\max_f} = \frac{(Pa_f + nPb_f)c_f}{I_f} \tag{23}$$

where the second term from Eq. (22) can be neglected because it is small compared to the first. The maximum stress in the stiff beam is

$$\sigma_{\max_s} = \frac{(Pa_f + nPb_f + PL_s)c_s}{I_s} \tag{24}$$

For the maximum stress in the entire beam to be in the thinner segment (i.e., $\sigma_{\max} = \sigma_{\max_f}$), the maximum stress in the flexure has to be greater than the maximum stress in the stiffer segment or

$$\frac{(Pa_f + nPb_f)c_f}{I_f} > \frac{(Pa_f + nPb_f + PL_s)c_s}{I_s} \tag{25}$$

For a rectangular cross section, $c_f = h_f/2$ and $I_f = w_f h_f^3/12$ and $c_s = h_s/2$ and $I_s = w_s h_s^3/12$. Substituting these values into the above

equation and solving for h_s produces

$$\sigma_{\max} = \sigma_{\max_f} \text{ if } h_s > h_f \sqrt{\frac{w_f}{w_s}\left(1 + \frac{L_s}{a_f + nb_f}\right)} \tag{26}$$

For a circular cross section, $c_f = r_f/2$ and $I_f = \pi/4 r_f^4$ and $c_s = r_s/2$ and $I_s = \pi/4 r_s^4$. Substituting these values into the above equation and solving for r_s produces

$$\sigma_{\max} = \sigma_{\max_f} \text{ if } r_s > r_f \sqrt{[3]}\left(1 + \frac{L_s}{a_f + nb_f}\right) \tag{27}$$

If Eq. (26) or Eq. (27) is not satisfied, the maximum stress occurs at the wall as given in Eq. (24). Using the MBM, another formulation of the stress at the wall is given by

$$\sigma_{\max_s} = \frac{(FL_{sy} + M_{ts})c_s}{I_s} \tag{28}$$

2.2.2 Deflection Loads. In the case of a deflection load, i.e., b is given, Eq. (16) has two unknowns, F and Θ_f. In the PRBM, Eq. (6) relates the force to the pseudo-rigid angle. We can create a variant of that equation for the deflection load case, given as

$$Fl_f \gamma \cos(\Theta_f + \theta_s) = \gamma K_{\Theta f} \frac{E_f I_f}{l_f} \Theta_f \tag{29}$$

We now have two equations (Eqs. (16) and (29)) and two unknowns (F and Θ_f) and can therefore solve for the force and Θ_f which can be used in Eq. (17) to solve for the second endpoint location a. The maximum stress can then be determined using the conditions stated in Sec. 2.2.1.

2.2.3 Force Loads. For force loads, i.e., F, is given, Eq. (16) has two unknowns, b and Θ_f. Here, we can use Eq. (29) to solve for Θ_f directly and use that value in Eq. (16) to solve for b and Eq. (17) to solve for a. Once again, the maximum stress can then be determined using the conditions stated in Sec. 2.2.1.

2.3 Numerical Boundary Value Problem Analysis. The governing differential equation for the large deflection of a cantilever beam with end loads consisting of both forces and a moment can be solved numerically as a BVP. In this formulation, bending is considered to be the dominant deformation with negligible shear and axial deformations. A numerical solution to this problem for constant cross sections is shown in Ref. [39]. This procedure can be extended to accommodate for variable cross sections.

Let a cantilever beam be represented by an arc length, s, along the flexure centerline as shown in Fig. 3(*a*), where s_l is the full arc length to the tip of the beam (note $s_l = l$). The Cartesian coordinates can be expressed as functions of arc length in terms of the angle of deflection $\theta(s)$ as

$$x(s) = \int_0^s \cos\theta(u)\mathrm{d}u, \quad y(s) = \int_0^s \sin\theta(u)\mathrm{d}u \tag{30}$$

The derivatives of these expressions are

$$\frac{\mathrm{d}x}{\mathrm{d}s} = \cos\theta(s), \quad \frac{\mathrm{d}y}{\mathrm{d}s} = \sin\theta(s) \tag{31}$$

Let the end tip location (a, b) be as shown in Fig. 3(*a*). Furthermore, let the forces on the end of a cantilever beam be denoted as F_x, F_y, and M_t representing the horizontal tip force, vertical tip force, and tip moment, where F_x and F_y are aligned with the coordinate directions and M_t is an applied counterclockwise moment. From the Euler–Bernoulli equation and an expression for the bending moment along the beam, $M(s)$, we can write

$$E(s)I(s)\frac{\mathrm{d}\theta}{\mathrm{d}s} = M(s) = -F_x(b - y(s)) + F_y(a - x(s)) + M_t \tag{32}$$

where $I(s)$ is the moment of inertia and $E(s)$ is the modulus of elasticity, both as functions of arc length.

Taking the derivative of Eq. (32) and then substituting from Eq. (31) results in the following second-order nonlinear differential equation

$$\frac{\mathrm{d}^2\theta}{\mathrm{d}s^2} = \frac{1}{E(s)I(s)}\left[F_x \sin\theta - F_y \cos\theta - \frac{\mathrm{d}\theta}{\mathrm{d}s}\left(I(s)\frac{\mathrm{d}E(s)}{\mathrm{d}s} + E(s)\frac{\mathrm{d}I(s)}{\mathrm{d}s}\right)\right] \tag{33}$$

This can be rewritten as a system of first-order differential equations as

$$\frac{\mathrm{d}z_1}{\mathrm{d}s} = z_2$$

$$\frac{\mathrm{d}z_2}{\mathrm{d}s} = \frac{1}{E(s)I(s)}\left[F_x \sin z_1 - F_y \cos z_1 - z_2\left(I(s)\frac{\mathrm{d}E(s)}{\mathrm{d}s} + E(s)\frac{\mathrm{d}I(s)}{\mathrm{d}s}\right)\right] \tag{34}$$

where $z_1 = \theta$, $z_2 = \mathrm{d}\theta/\mathrm{d}s$, and the moment of inertia, $I(s)$, and modulus of elasticity, $E(s)$, are expressed as differentiable functions of the arc length. The boundary conditions that must be satisfied are

$$z_1(0) = 0, \quad z_2(s_l) = \frac{M_t}{E(s_l)I(s_l)} \tag{35}$$

The numerical solution to the problem can be found using a BVP solver such as MATLAB's *bvp5c* function. A piecewise cubic hermite interpolating polynomial (*pchip*) can be convenient to represent the moment of inertia and modulus of elasticity functions. After solving numerically for $\theta(s)$ or $z_1(s)$, numerical integration can be used with Eq. (30) to find the coordinates of the beam. To represent a step in cross section, five points were used in the *pchip* function, the endpoints of the beam, the location of the step, and the location of the step $\pm 0.01 L_t$. For the fixed endpoint and the location $-0.01 L_t$ from the step, the stiff values of I_s and E_s were used. For the loaded end and location $+0.01 L_t$ from the step, the flexible values of I_f and E_f were used. At the step location, the average value of I and E was used. The solution was calculated through a mesh of points along the entire beam length. A total of 150 points were used along the beam length in the analysis.

This process can be used to help validate the MBM as will be shown later on.

2.4 Finite Element Analysis. To validate the MBM, a large selection of force and displacement analyses were performed using FEA. Each analysis varied in some geometric value, loading condition, or material property. The parametric study parameters for the analyses are given in Tables 1 and 2 and an example image of an output from the FEA program is given in Fig. 11. All possible combination parameters from Tables 1 and 2 were analyzed. ANSYS 19.1 was used for the analysis. Geometric nonlinearities were included in all analyses. In total, 14,580 analyses were performed for each force and deflection loading condition on rectangular cross sections. The results from the FEA were used to compare the model predictions. The moduli of elasticity were picked to approximate three common materials. These materials and the accompanying tensile yield strengths used in the analysis are given in Table 3. If a material exceeded the yield strength in the FEA results, that sample was removed from the subsequent comparison to the MBM.

Circular cross-sectional stepped beams were also analyzed to show application in non-rectangular cross sections. The parametric study parameters for the analyses are given in Table 2. Six hundred and forty eight analyses were performed for both force and deflection loading conditions on circular cross sections.

To analyze the effect of steps in material properties, material changes at the step were introduced, as can be seen in the elastic moduli used shown in Tables 1 and 2. These cases had both a

Table 1 Rectangular cross sections FEA parametric study parameters

$Base_s$ (m)	$Height_s$ (m)	$Base_f$ (m)	$Height_f$ (m)	L_T (m)	$\frac{L_f}{L_s}$	E_s (Pa)	E_f (Pa)	Force (N)	Deflection (m)
0.011	0.003	0.011	0.0005	0.025	0.1	1.13×10^{11}	1.13×10^{11}	10	0.006
0.013	0.004	0.013	0.001	0.05	0.3	1.93×10^{11}	1.93×10^{11}	30	0.008
0.015	0.005	0.015		0.075	0.5		4.50×10^{9}	50	0.01
					0.7				
					0.9				

Table 2 Circular cross sections FEA parametric study parameters

$Radius_s$ (m)	$Radius_f$ (m)	L_T (m)	$\frac{L_f}{L_s}$	E_s (Pa)	E_f (Pa)	Force (N)	Deflection (m)
0.0015	0.00025	0.025	0.1	1.13×10^{11}	1.13×10^{11}	0.05	0.006
0.002	0.0005	0.05	0.5	1.93×10^{11}	1.93×10^{11}	0.1	0.01
0.0025		0.075	0.9		4.50×10^{9}		

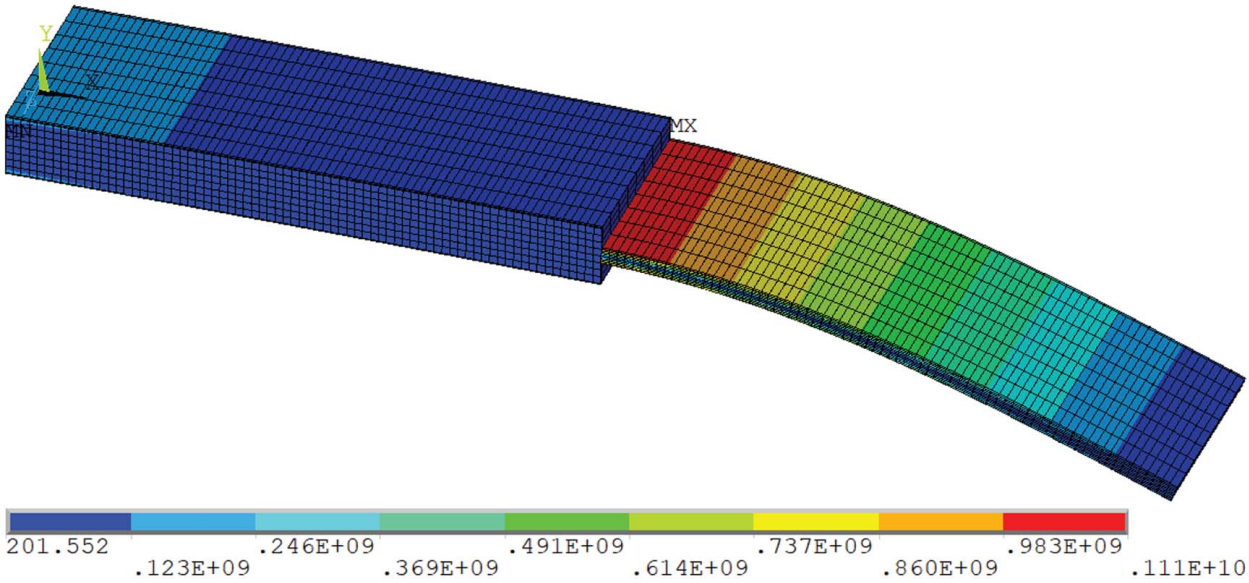

Fig. 11 Example image from FEA output. Von Mises stresses are plotted, and the maximum is marked (point MX) as the transition between the flexible and stiff beams, as expected. Parameters for image: $L_s = L_f = 0.075/2$, $E_s = E_f = 1.13\times10^{11}$, $Base_s = Base_f = 0.013$, $Height_s = 0.004$, $Height_f = 0.001$, and Force = 100, units as stated in Table 1 with FEA results in Pa.

Table 3 Material properties

Material	E (Pa)	σ_y (Pa)	ν
Ti-64	1.13×10^{11}	8.8×10^{8}	0.342
316 SS	1.93×10^{11}	2.9×10^{8}	0.27
PEEK	4.50×10^{9}	9.0×10^{7}	0.4

step of geometry and material properties. The case of just a step of material with no geometry change was also tested with the first step being the Ti-64 simulated material and the second step being the simulated polyetheretherketone (PEEK) material. A selection of lengths, ratios, and dimensions similar scale to those used in Tables 1 and 2 was used in the validation.

For each of the FEA models, the beam was meshed with 75 divisions along each step length, resulting in 150 divisions along the beam, as was used in the BVP. The cross section was divided into a 10×10 grid of elements for each division.

For each of the loading cases analyzed that remained below the yield stress, the rigid assumption model and the MBM were run for comparison. The error between the model and the FEA result was calculated by

$$\text{error} = \left(\left|\frac{X_{\text{MODEL}} - X_{\text{FEA}}}{X_{\text{FEA}}}\right|\right) * 100\% \tag{36}$$

and averaged for all the analyses. Due to the possibility of subtraction and round-off error, deflections under 10^{-6} were removed from the error analysis. This became particularly necessary for evaluating the deflections of b_s and θ_s. When analyzing the force load cases, only b deflections greater than the thickness of the flexible member h_f were considered as any deflection less than that would be a small deflection and other analytical solutions such as Castigliano's second theorem could be used. Equation (36) was also used to compare the MBM to the BVP solution and physical prototype results.

2.5 γ, c_Θ, and K_Θ Optimization. Since there is not an analytical solution to compare against, optimization of the model parameters γ, c_Θ, and K_Θ used in the MBM was performed against both the FEA and the BVP solutions to see the influence on the

respective error. The optimal values for γ, c_Θ, and K_Θ for the MBM are then provided for best approximating the FEA and BVP solutions. The optimization was performed by minimizing the absolute value of the sum errors of each of the measured values (angles, deflections, forces to deflect, stress) for the rectangular stepped geometry case. Therefore, the optimized parameters apply to all evaluated loadings, material properties, and geometries tested, not individual cases. This was done in an effort to provide a universal set of parameters for the best results regardless of the scenario. MATLAB's constrained optimizer function, *fmincon*, was used with an active-set algorithm.

2.6 Prototype Development. In addition to computational analysis, physical prototypes were constructed and tested to validate the MBM. Aluminum 6061-T6 beams were cut using wire-electrical discharge machining (EDM). Three sample sets were made, with the step at 25%, 50%, and 75% of the total length with ten samples in each set. All 30 samples were 6.5 mm wide with a stiff segment height of 3 mm and a flexible segment height of 1 mm. A 2 cm long 5 mm high clamping area was manufactured into the beam as well as a millimeter diameter hole at the end to attach a mass. The total length of each beam or the length from the clamping area to the loading hole was 15 cm. Each of the three sample sets were loaded with calibrated masses attached by a metal wire. The loads were selected to approach the yielding stress and obtain a large endpoint deflection for each beam. As such, for the 25/75 stiff/flexible beams a 200 g load was used, for the 50/50 beams 400 g was used, and for the 75/25 beams 700 g was used. The wire used to attach the masses had a mass of less than 1 g. Pictures were taken (resolution of 6000×4000 pixels taken from a distance to result in approximately 30 pixels/mm) of the loaded and unloaded case for each sample and pixel locations were used to determine the deflections and angles under load. An example of images taken can be seen in Fig. 12.

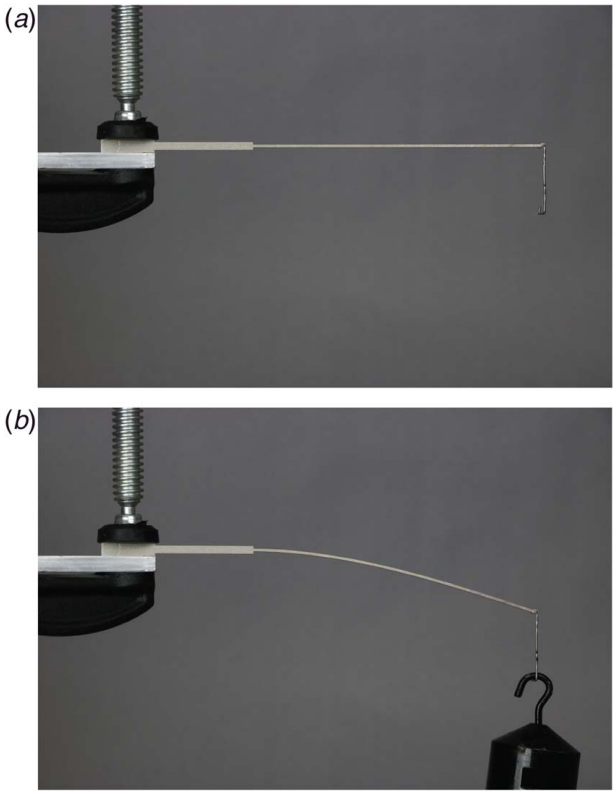

Fig. 12 Wire-EDM cut prototype example, 25% stiff 75% flexible from aluminum 6061-T6: (*a*) unloaded and (*b*) loaded (200 g)

3 Results and Discussion

The errors of the model predictions as compared to the other analysis methods are given here, comparing both the rigid assumption model and the MBM. A discussion on computational expense is also provided. Benefits and limitations of the MBM identified during the comparison are presented.

3.1 Error Results in Comparing Models With Finite Element Analysis, Boundary Value Problem, and Linear Solutions. In the comparison of the FEA results to the MBM, seven variables were compared. In the case of deflection loads, of the 14,580 samples with rectangular cross sections, 3997 samples were under the yield stress and used in the comparison. The errors can be found in Table 4. The average error between the model prediction over the 3997 samples along with the standard deviation (SD) is reported. The maximum absolute value error value is also reported. The model was then optimized to the FEA solution and the errors are again reported using the optimized values of γ, K_Θ, and c_θ. For the rigid assumption, four of the seven parameters (those parameters not involving the stiffened segments of the beam) are compared. An optimization was also performed and reported to see if the rigid assumption could simply be used if optimizing the parameters in the PRBM.

For force loads, of the 14,580 samples with rectangular cross sections, 2115 samples were under the yield stress and deflection criteria. For all 2115 force-loaded samples with rectangular cross sections, the MBM was compared to the BVP solution. The BVP solution was also compared to the FEA results. A summary of the errors is shown in Table 5. As in the case of deflection loads, average error between the model prediction over the 2115 samples under the yield and deflection criteria is reported, along with the SD and maximum absolute value error term.

For circular cross sections under deflection loads, of the 648 samples, 108 samples were under the yield stress and used in comparison. Under force loads, of the 648 samples, 462 samples were under the yield stress. Error ranges were similar in the case of circular cross sections as those found in the rectangular cases. The optimization was run with just the rectangular solutions but the optimal values still provided dramatic reductions in errors (approximately 4% average to approximately 0.5% average) similar to those seen in rectangular solutions.

For just steps in material properties at a constant cross section, 180 samples were analyzed for force and deflection loads. Thirteen and 38 of the cases, respectively, remained under yield. The error ranges for the cases tested remained below the values for stepped geometries.

From Tables 4 and 5, we can see that the MBM closely approximates the finite element solution in all cases. When the values of γ, K_Θ, and c_θ are optimized to the FEA solution, there is little difference between the two solutions. The rigid assumption has the potential for large errors, especially in parameters such as determining force, angle of deflection, stress in deflection load cases, stress in force load cases, and vertical deflection, b. When optimizing the rigid assumption to the FEA, little improvement is seen but the solution remains less accurate than the MBM. The MBM compares to the BVP better than the FEA results by a small margin. The BVP solution was also run at a higher refinement (1000 points along the length) to see if the higher refinement reduced the errors relative to the MBM and FEA solutions. The higher refinement did bring the solutions towards the FEA and MBM by reductions in the errors of approximately 1% in the average values and 2–4% in the maximum errors but at an increase of about $10x$ to the computational cost. Optimizing for the BVP provided little improvement, indicating that the original PRBM values are close to optimal for this case. In optimizing both to the BVP and the FEA solutions, γ and K_Θ were reduced in both cases. c_θ made no change for the BVP as θ_f was not calculated, but for the FEA optimization, it deceased from 1.2385 to 1.2196.

Table 4 Percent error for rectangular cross section under deflection loads

		% Error using PRBM parameters			% Error using optimized parameters		
		Average (%)	SD (%)	Max (%)	Average (%)	SD (%)	Max (%)
MBM to FEA	F	4.01	0.65	5.05	0.21	0.31	2.42
	a	0.06	0.05	0.58	0.05	0.07	0.58
	a_s	<0.01	0.03	0.60	<0.01	0.03	0.60
	b_s	3.02	0.94	4.57	1.09	1.01	5.97
	θ_f	3.03	0.39	5.19	0.37	0.35	2.49
	θ_s	4.05	0.62	5.09	0.23	0.32	2.44
	σ	4.79	0.62	5.86	0.59	0.22	1.70
Rigid assumption to FEA	F	40.18	734.20	19,962.86	20.00	356.97	9721.64
	a	0.05	0.26	5.23	0.34	0.38	3.62
	θ_f	5.13	45.71	979.78	2.68	41.92	896.05
	σ	18.73	275.86	5847.78	10.68	182.43	3866.00
Linear to FEA	F	4.81	4.25	21.05			
	a	1.94	1.86	12.97			
	a_s	<0.01	0.03	0.60			
	b_s	4.82	4.40	28.54			
	θ_f	0.95	0.85	4.26			
	θ_s	2.71	2.74	16.08			

Note: Sample size of 3997.

Table 5 Percent error for rectangular cross section under force loads

		% Error using PRBM parameters			% Error using optimized parameters		
		Average (%)	SD (%)	Max (%)	Average (%)	SD (%)	Max (%)
MBM to FEA	b	3.66	1.13	5.28	0.22	0.19	1.55
	a	0.11	0.15	0.69	0.04	0.10	0.88
	a_s	0.00	0.01	0.06	<0.01	<0.01	0.06
	b_s	0.98	1.13	7.70	1.10	1.16	7.79
	θ_f	5.24	1.24	7.77	0.22	0.29	2.21
	θ_s	0.10	0.16	0.96	0.13	0.14	1.31
	σ	0.66	0.23	1.58	0.60	0.12	0.91
Rigid assumption to FEA	b	14.71	22.40	98.90	12.00	22.94	98.85
	a	0.09	0.11	0.54	0.13	0.18	0.81
	θ_f	6.60	1.24	7.77	0.22	0.29	2.21
	σ	1.09	2.52	33.82	1.15	2.52	33.82
MBM to BVP	b	2.61	3.38	26.53	2.55	3.41	26.57
	a	0.05	0.07	0.47	0.03	0.06	0.54
	a_s	3.25	4.25	11.07	3.25	4.25	11.07
	b_s	3.53	6.03	21.08	3.52	6.01	20.92
FEA to BVP	b	5.40	3.75	30.19			
	a	0.07	0.12	0.87			
	a_s	3.26	4.25	11.07			
	b_s	3.72	6.52	26.98			
Linear to FEA	b	3.02	6.70	52.75			
	a	1.26	2.99	24.38			
	a_s	0.00	0.01	0.06			
	b_s	2.48	3.94	24.22			
	θ_f	2.48	5.32	41.75			
	θ_s	1.44	3.26	26.31			

Note: Sample size of 2115.

Table 6 includes the optimized values and the PRBM values for comparison. As the values for both γ and K_Θ are reduced and those for γ are so similar, it is likely that the true optimal values for these parameters are also reduced from the pure vertical parameters in the PRBM. These results can show trends while an analytical solution would be required to find the true optimal values.

In both loading conditions, as expected, the linear solution maintains a high accuracy at lower deflections. This accuracy begins to diverge as deflection increases. This can be seen in the large maximum errors and large SDs from the average in Tables 4 and 5. This becomes clear when plotting the error in key results such as F for displacement loads and b for force loads against angular deflection at the endpoint, θ_f. This is shown in Fig. 13. The MBM decreases in error under larger deflections.

3.2 Comparison of Physical Results and Mixed-Body Model, Finite Element Analysis, and Boundary Value Problem Results. The physical test results were obtained using pixel locations and therefore values of a, b, a_s, b_s, θ_f, and θ_s could be obtained. These could then be compared to the FEA, BVP, and MBM solutions. The MBM used the pure vertical PRBM values for γ, K_Θ, and c_θ. These model solutions were compared to the average of the physical sample set solution. Inherent

Table 6 Optimized parameters for the MBM shown side-by-side with the PRBM parameters

Parameter	PRBM	MBM_{FEA}	MBM_{BVP}
γ	0.8517	0.8130	0.8144
K_Θ	2.6762	2.4416	2.5548
c_θ	1.2385	1.2196	1.2385

Notes: Two optimizations were performed, the MBM compared to the FEA solution, indicated by the subscripts, and the MBM to the BVP solution. There was no change to c_θ in the optimization of the MBM to the BVP solution as the BVP solution did not contain results for θ_s and θ_f.

error is expected to be introduced in the physical results from the measurement methods. These were recorded as follows. The samples were measured using calipers to ensure manufacturing resulted in the desired dimensions. The resolution of the calipers was ±0.1 mm. The pixel/millimeter measurement introduced a second resolution error of approximately ±0.04 mm. As the loading was in the direction of gravity, the self weight of the beam also provides an additional load, altering endpoint locations up to an additional 0.5 mm. The cumulative measurement uncertainties plus the SD of the sample set were then added and used to create a percent error range due to measurement. The model errors when compared to the average physical test result, along with the percent error range from measurement, are shown in Table 7.

From Table 7, we see that the MBM performs similarly to the other two methods of analysis. It strays outside the percent measurement error range for b, a_s, and θ_f but in each case by less than a percent. Using optimized parameters for γ, K_Θ, and c_θ creates error results similar to the FEA case, removing the instances that stray outside the measurement error range except in the case of a_s which remains a tenth of a percent outside the measurement error. This further indicates that the optimal parameters for the model are close to those obtained in the FEA and BVP optimizations.

3.3 Mixed-Body Model Benefits and Limitations. The primary benefit of the MBM is a simple, computationally inexpensive way of analyzing large deflections in stepped cantilever beams. The MBM provides a robust approach to different geometries and material properties. While the equations are more involved, the computational expense is similar to that of the PRBM. Additionally, the computational expense of the MBM is much less than both FEA or the BVP presented above. The times to run the FEA solution on ANSYS averaged approximately 1.6 s per evaluation, BVP on MATLAB timed at approximately 4.5 s per evaluation, and the MBM (coded in MATLAB) at approximately 0.04 s per evaluation using the same computer and processor. This results in evaluations 40 × faster than FEA and 112 × faster than the BVP.

The maximum and average errors in the MBM are equal or lower for all the cases when compared to the rigid assumption predictions and are more robust to all large-deflection situations. The stress prediction was often over-predicted by a small percentage. While this is a limitation in analyzing failures, it can be a benefit in design by having slightly conservative stress predictions. A limitation here is the model does not account for the stress concentration at the step. A stress concentration factor could be added to the stress prediction when specific geometry is known.

As an approximate analytical solution to the problem, the MBM introduces some slight error into the results. These errors are typically lower than 5% and often much lower when compared to the other methods of analysis. While this error could be a limitation in fine-tuned design, the computational speed of the analysis lends better to optimization problems where large numbers of computations are required.

When comparing against the linear solution, the optimized MBM parameters showed equivalent performance at low deflections while also providing a similar amount of accuracy at high deflections where the linear assumption breaks down. At low deflections, the increased complexity of the model does not justify replacement of standard models such as Castigliano's theorem but the wide range of accuracy of the MBM does allow for use cases that span both large and small deflections without necessitating transitions between models. An advantage of the MBM is the ability to easily accommodate both changes to moment of inertia and material properties at the step. This could extend the usage of the MBM to cases where the moment of inertia does not change but the beam material properties change from a stiff to a flexible member at a discrete point along the length.

Limitations to the MBM are primarily seen in inaccuracies which begin to be introduced in very high deflections of the flexible beam. This is observed in the PRBM and results in limits on accuracy for

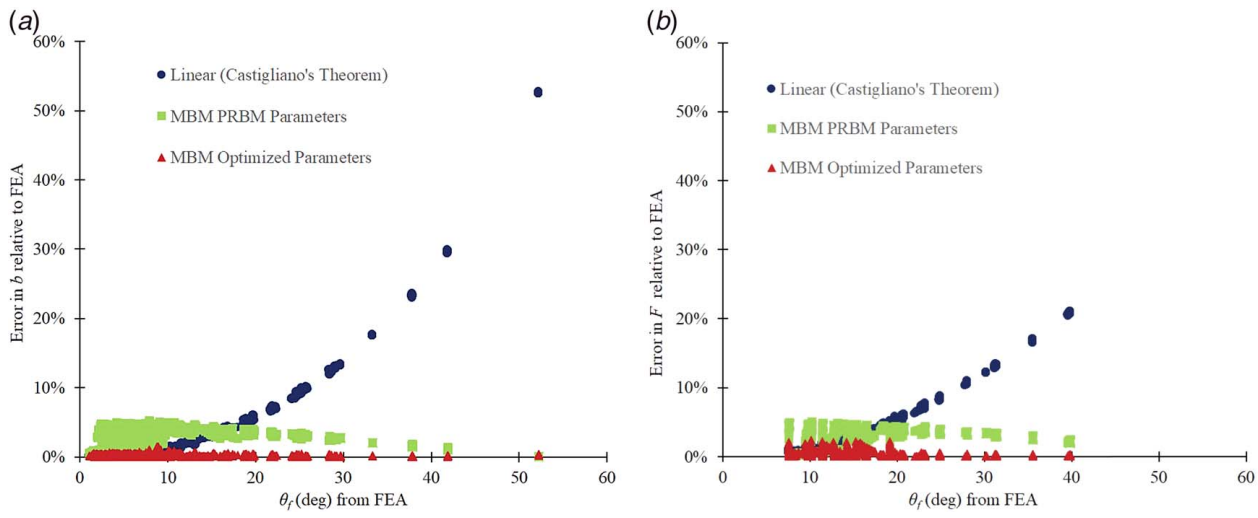

Fig. 13 Error by end angle comparison between the MBM and the linear assumption solutions. It can be seen that the MBM becomes more accurate to the FEA solution at larger angular deflections where the linear assumption becomes clearly unsuitable for accurate modeling. The optimized MBM parameters provide solutions equivalently accurate to the linear solution through small deflections while maintaining that level of accuracy through any end angle. (*a*) Comparisons of error between the MBM and the linear assumption for force loads for the values of *b* and (*b*) comparisons of error between the MBM and the linear assumption for deflection loads for the values of *F*.

Table 7 Percent error for rectangular cross-sectional physical prototypes under force loads

	MBM to physical (optimized) (%)	FEA to physical (%)	BVP to physical (%)	Measurement error (%)
b	3.20 (1.37)	1.42	3.23	2.76
a	0.48 (0.48)	0.67	0.61	1.08
a_s	1.41 (1.41)	1.46	0.98	1.32
b_s	21.39 (21.06)	19.87	18.15	39.68
θ_f	3.99 (2.36)	2.46	N/A	3.68
θ_s	15.48 (15.48)	15.39	N/A	22.26

Note: Sample size of 30. The optimized solution of the MBM used the parameters obtained by optimizing to the FEA solution.

force and position predictions. As θ_f approaches $\pi/2$, the pure vertical load results in less of a bending load and more tensile and shear loading, resulting in an exponential increase in error. Therefore, these limits are values of Θ_f that define when the error exceeds a given value. For the MBM, a similar limit can be observed. However, given the contribution of θ_s, these values will be lower than those limits in the PRBM. For the optimized parameters, the error can be kept below the maximum errors shown in Tables 4 and 5 for force and position predictions when limits of approximately 85% of those given by the PRBM are used. Therefore, for force and end-position, respectively, the MBM remains under the maximum errors of 2.42% and 1.55% when Θ_f does not exceed approximately 0.87 and 0.96 radians (50 deg and 55 deg).

The MBM is also limited to cases where the stiffness in the segment attached to the wall is greater than that in the second segment as the majority of bending should occur in the second segment. The current model has only been validated in pure vertical loads. Further validation will be needed to ensure accurate predictions when additional loads are applied, such as horizontal loads or moments.

4 Conclusion

In this work, a method for predicting large deflections of stepped cantilever beams is presented. This method, the MBM, builds on a mixture of small-deflection assumptions and the PRBM for large deflections. The model uses a combination of the equations provided by both methods of analysis and creates a model that can predict the endpoint locations, stress, and force to deflect a stepped beam under vertical end loads. The MBM can be used for both step changes in geometry or material properties or combinations of both cases. The model was compared to FEA results and maintained a low average error over a large sample of loadings, geometries, and material properties. The model has less error than a simple assumption that the first step in the beam is rigid. The MBM also provided significantly improved results over linear methods for large deflections while remaining accurate in small deflections. The MBM also compared well with numerical BVP solutions and testing of physical prototypes. The validation procedures evaluated a large number of loading cases, geometries, and material properties. In seeking a model that can be universally applicable to changes in these areas, optimization over all tested scenarios to find model parameters that best fit all cases was performed. This further reduced the average error between the MBM and numerical solutions. The maximum error and SD in results between changes in loading cases remained small, showing a model that is applicable to large ranges regardless of the scenario. Future work could analyze the specific effect of given loading cases, geometries, and material properties on the model accuracy and could result in model parameters optimized to specific scenarios for lower average error.

The MBM provides a simple method for analyzing stepped cantilever beams undergoing large deflections, which can be helpful in design where many iterations are often necessary. This shows promise for use in the design of medical implants, which motivated the development of the MBM. A primary motivation for this work, a compliant-mechanism-based medical device, is not disclosed here but is a part of ongoing work. Other areas of future work will include expanding the model to other loading conditions such as mixed vertical and horizontal loading in the fixed-free case, a fixed-guided end condition, precurved beams, and pure end-moments which would increase the applicability of the MBM. PRBMs exist for these loading conditions and future research will ensure that the assumptions used in the load case presented here also provide accurate solutions for these other cases.

Acknowledgment

This paper is based on work supported by the U.S. National Science Foundation through NSF [Grant No. 1663345] and a grant by Zimmer-Biomet in conjunction with Cincinnati Children's Hospital Medical Center.

Conflict of Interest

There are no conflicts of interest.

Data Availability Statement

The authors attest that all data for this study are included in the paper.

Nomenclature

a = endpoint position in the horizontal direction
b = endpoint position in the vertical direction
c = distance from the neutral axis to the most extreme beam fiber
h or Height = cross-sectional dimension of a segment perpendicular to the axis of bending
l = lowercase l indicates the length of a segment considered to be undergoing large deflections
r = radius
s = position along a beam, measured along the neutral axis from the wall
w or Base = cross-sectional dimension of a segment along the axis of bending
E = modulus of elasticity
F = force
I = moment of inertia of the cross section
L = uppercase L indicates the length of a segment considered to be undergoing small deflections
M = moment
P = force that acts perpendicular to the unbent beam
c_θ = non-dimensional parameter used in modeling angles
K_Θ = non-dimensional parameter used in modeling torques
$L_{s\gamma}$ = length of the beam from the wall to the characteristic pivot
M_{ts} = theoretical moment of the torsional spring at the pseudo-rigid characteristic pivot
nP = force that acts parallel to the unbent beam

Greek Symbols

γ = non-dimensional parameter used in modeling lengths
δ = deflection
θ = angle of the actual segment at a given point
Θ = angle of the pseudo-rigid link

ν = Poisson's ratio
σ = stress
σ_y = yield stress

Subscripts

s = a value relative to the first, stiffer segment attached to the wall
f = a value relative to the second, more flexible segment further from the wall

References

[1] Sanchez-Marin, F., Roda-Casanova, V., and Porras-Vazquez, A., 2018, "A New Analytical Model to Predict the Transversal Deflection Under Load of Stepped Shafts," Int. J. Mech. Sci., **146**, pp. 91–104.
[2] Liu, Z., Song, W., and Lu, Q., 2017, "A Piece-Wise Beam Model for Shafts With Abrupt Changes of Section in Gearbox Products," International Conference on Advanced Mechatronic Systems (ICAMechS), Xiamen, China, Dec. 6–9, IEEE, pp. 318–323.
[3] Diwan, A. A., Al-Ansari, L. S., Al-Saffar, A. A., and Al-Anssari, Q. S., 2019, "Experimental and Theoretical Investigation of Static Deflection and Natural Frequency of Stepped Cantilever Beam," Aust. J. Mech. Eng., pp. 1–13.
[4] Li, S.-C., Liang, L., and Yu, Q., 2019, "Natural Frequency of Bending Vibration for Stepped Beam of Different Geometrical Characters and Materials," Noise Vib. Worldwide, **50**(1), pp. 3–12.
[5] Ahmed, E., Tamer, E., and Said, F., 2020, "Optimal Design for Maximum Fundamental Frequency and Minimum Intermediate Support Stiffness for Uniform and Stepped Beams Composed of Different Materials," Technical Report, SAE Technical Paper.
[6] Wattanasakulpong, N., and Chaikittiratana, A., 2016, "Adomian-Modified Decomposition Method for Large-Amplitude Vibration Analysis of Stepped Beams With Elastic Boundary Conditions," Mech. Based Des. Struct. Mach., **44**(3), pp. 270–282.
[7] Hamidizadeh, H., Mashhadi, M. M., and Mohammadi, Y., 2020, "Static Pull in Analysis of Stepped Microcantilever Beam Based on Strain Gradient Theory Using Differential Quadrature Method," Mech. Based Des. Struct. Mach., **49**(7), pp. 1–14.
[8] Ashok, A., Gangele, A., Pal, P., and Pandey, A. K., 2018, "An Analysis of Stepped Trapezoidal-Shaped Microcantilever Beams for MEMS-Based Devices," J. Micromech. Microeng., **28**(7), p. 075009.
[9] Zhang, J., Song, A., Xu, X., and Lu, W., 2016, "A Rigid and Flexible Structures Combined Deployable Boom for Space Exploration," IEEE International Workshop on Intelligent Robots and Systems (IROS), Daejeon, South Korea, Oct. 9–14, IEEE, pp. 2920–2926.
[10] Mikulas, M. M., Pappa, R. S., Warren, J., and Rose, G., 2015, "Telescoping Solar Array Concept for Achieving High Packaging Efficiency," 2nd AIAA Spacecraft Structures Conference, Kissimmee, FL, Jan. 5–9, p. 1398.
[11] Prajapati, S., Gupta, V., and Mukherjee, S., 2017, "Mathematical Modelling of Stepped Beam Energy Harvesting Using Euler–Bernoulli's Theory," International Conference on Physics and Mechanics of New Materials and Their Applications, Jabalpur, India, Oct. 14–16, Springer, pp. 549–565.
[12] Usharani, R., Uma, G., Umapathy, M., and Choi, S.-B., 2018, "A Novel Piezoelectric Energy Harvester Using a Multi-stepped Beam With Rectangular Cavities," Appl. Sci., **8**(11), p. 2091.
[13] Terrazas, C. A., Gaytan, S. M., Rodriguez, E., Espalin, D., Murr, L. E., Medina, F., and Wicker, R. B., 2014, "Multi-material Metallic Structure Fabrication Using Electron Beam Melting," Int. J. Adv. Manuf. Technol., **71**(1), pp. 33–45.
[14] Desbiolles, B., Bertsch, A., and Renaud, P., 2019, "Ion Beam Etching Redeposition for 3d Multimaterial Nanostructure Manufacturing," Microsyst. Nanoeng., **5**(1), pp. 1–8.
[15] Hiller, J. D., and Lipson, H., 2009, "Multi Material Topological Optimization of Structures and Mechanisms," 11th Annual Conference on Genetic and Evolutionary Computation, Montreal, Quebec, Canada, July 8–12.
[16] Mattiasson, K., 1981, "Numerical Results From Large Deflection Beam and Frame Problems Analysed by Means of Elliptic Integrals," Int. J. Numer. Methods Eng., **17**(1), pp. 145–153.
[17] Howell, L. L., 2001, *Compliant Mechanisms*, John Wiley & Sons, New York.
[18] Wang, Z., Sun, H., Wang, B., and Wang, P., 2020, "Adaptive Pseudo-Rigid-Body Model for Generalized Cross-Spring Pivots Under Combined Loads," Adv. Mech. Eng., **12**(12), p. 1687814020966539.
[19] Venkiteswaran, V. K., and Su, H.-J., 2016, "Pseudo-Rigid-Body Models for Circular Beams Under Combined Tip Loads," Mech. Mach. Theory, **106**, pp. 80–93.
[20] Venkiteswaran, V. K., and Su, H.-J., 2018, "A Versatile 3r Pseudo-Rigid-Body Model for Initially Curved and Straight Compliant Beams of Uniform Cross Section," ASME J. Mech. Des., **140**(9), p. 092305.
[21] Awtar, S., and Sen, S., 2010, "A Generalized Constraint Model for Two-Dimensional Beam Flexures: Nonlinear Load-Displacement Formulation," ASME J. Mech. Des., **132**(8), p. 02005.
[22] Li, S., Hao, G., Chen, Y., Zhu, J., and Berselli, G., 2021, "Nonlinear Analysis of a Class of Inversion-Based Compliant Cross-Spring Pivots," ASME J. Mech. Rob., **14**(3), p. 031007.
[23] Ma, F., and Chen, G., 2014, "Chained Beam-Constraint-Model (CBCM): A Powerful Tool for Modeling Large and Complicated Deflections of Flexible Beams in Compliant Mechanisms," ASME 2014 International Design Engineering Technical Conferences and Computers and Information in Engineering Conference, Buffalo, NY, Aug. 17–20, American Society of Mechanical Engineers, p. V05AT08A027.
[24] Shigley, J. E., 2015, *Shigley's Mechanical Engineering Design*, Tata McGraw-Hill Education, New York.
[25] Yoo, W.-S., Park, S.-J., Park, J.-Y., and Sohn, J.-H., 2004, "Physical Experiments and Computer Simulations of a Stepped Cantilever Beam With a Hybrid Coordinate Formulation," Mech. Based Des. Struct. Mach., **32**(4), pp. 515–532.
[26] Holst, G. L., Teichert, G. H., and Jensen, B. D., 2011, "Modeling and Experiments of Buckling Modes and Deflection of Fixed-Guided Beams in Compliant Mechanisms," ASME J. Mech. Des., **133**(5), p. 051002.
[27] Zhang, A., and Chen, G., 2013, "A Comprehensive Elliptic Integral Solution to the Large Deflection Problems of Thin Beams in Compliant Mechanisms," ASME J. Mech. Rob., **5**(2), p. 021006.
[28] Frisch-Fay, R., 1962, *Flexible Bars*, Butterworths, London.
[29] She, Y., Gu, Z., Song, S., Su, H.-J., and Wang, J., 2021, "Design, Modeling, and Manufacturing of a Variable Lateral Stiffness Arm Via Shape Morphing Mechanisms," ASME J. Mech. Rob., **13**(3), p. 031020.
[30] Nielson, A. J., and Howell, L. L., 2001, "An Investigation of Compliant Micro-Half-Pantographs Using the Pseudorigid Body Model," Mech. Based Des. Struct. Mach., **29**(3), pp. 317–330.
[31] Su, H.-J., 2009, "A Pseudorigid-Body 3R Model for Determining Large Deflection of Cantilever Beams Subject to Tip Loads," ASME J. Mech. Rob., **1**(2), p. 021008.
[32] Marković, K., and Zelenika, S., 2017, "Optimized Cross-Spring Pivot Configurations With Minimized Parasitic Shifts and Stiffness Variations Investigated Via Nonlinear FEA," Mech. Based Des. Struct. Mach., **45**(3), pp. 380–394.
[33] Seymour, K., Bilancia, P., Magleby, S., and Howell, L., 2021, "Hinges and Curved Lamina Emergent Torsional Joints in Cylindrical Developable Mechanisms," ASME J. Mech. Rob., **13**(3), p. 031002.
[34] Gou, Y., Chen, G., and Howell, L. L., 2019, "A Design Approach to Fully Compliant Multistable Mechanisms Employing a Single Bistable Mechanism," Mech. Based Des. Struct. Mach., **49**(7), pp. 1–24.
[35] Jin, M., Yang, Z., Ynchausti, C., Zhu, B., Zhang, X., and Howell, L. L., 2020, "Large-Deflection Analysis of General Beams in Contact-Aided Compliant Mechanisms Using Chained Pseudo-Rigid-Body Model," ASME J. Mech. Rob., **12**(3), p. 031005.
[36] Verotti, M., 2020, "A Pseudo-Rigid Body Model Based on Finite Displacements and Strain Energy," Mech. Mach. Theory, **149**, p. 103811.
[37] Bagivalu Prasanna, P., Bapat, S. G., Midha, A., and Lodagala, V., 2020, "A Methodology for Determining Static Mode Shapes of a Compliant Mechanism Using the Pseudo-Rigid-Body Model Concept and the Degrees-of-Freedom Analysis," ASME J. Mech. Rob., **12**(2), p. 021115.
[38] Bilancia, P., Berselli, G., Bruzzone, L., and Fanghella, P., 2019, "A CAD/CAE Integration Framework for Analyzing and Designing Spatial Compliant Mechanisms Via Pseudo-Rigid-Body Methods," Rob. Comput.-Integr. Manuf., **56**, pp. 287–302.
[39] Bailey, N., Lusty, C., and Keogh, P., 2018, "Nonlinear Flexure Coupling Elements for Precision Control of Multibody Systems," Proc. R. Soc. A: Math. Phys. Eng. Sci., **474**(2218), p. 20180395.